

1

Supplementary Information

2 Self-assembly of CO₂-responsive surfactant solutions: from density 3 functional to molecular dynamics studies

4 Hao Luo ^a, Ming Zhou ^{a,b,*}, Jian Wang^{c,*}, Jingxin Hung ^a; Yijun Zhou ^d, Yi Li ^a, Chengyiting Li ^a,
5 Xingji Chen ^a.

6 ^a School of New Energy and Material, Southwest Petroleum University, Chengdu, Sichuan 610500,
7 China

8 ^b State Key Laboratory of Oil and Gas Reservoir Geology and Exploitation, School of New Energy
9 and Materials, Southwest Petroleum University, Chengdu Sichuan 610500, China

10 ^c College of Food and Biological Engineering, Chengdu University, Chengdu 610106, China

11 ^d China West Normal Univ, Coll Chem & Chem Engn, Nanchong 637000, People's Republic of
12 China

13

14 * Corresponding author

15 Ming Zhou and Jian Wang

16 Full postal address:

17 Southwest Petroleum University, Chengdu, Sichuan 610500, China

18 E-mail addresses:

19 mr.zhouming@163.com; wangjian@cdu.edu.cn

20

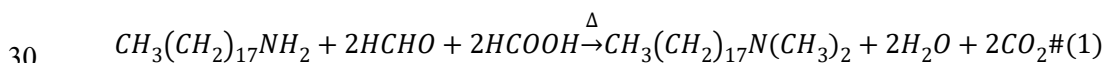
21 1. Synthesis and characterization of tertiary octadecylamine (DMA18)

22 1.1. materials

23 Formic acid, formaldehyde, sodium Salicylate, sodium hydroxide, and anhydrous ethanol were
24 purchased from Chengdu Cologne Co., Ltd, China, and octadecylamine (DMA) was purchased from
25 Shanghai Aladdin Biochemical Technology Co. All chemical reagents were analytically pure.

26 1.2 Synthesis

27 The CO₂-responsive surfactant tertiary octadecylamine (DMA18) was synthesized by
28 alkylation of octadecylamine with formic acid and formaldehyde, with the following synthetic
29 scheme in follow:

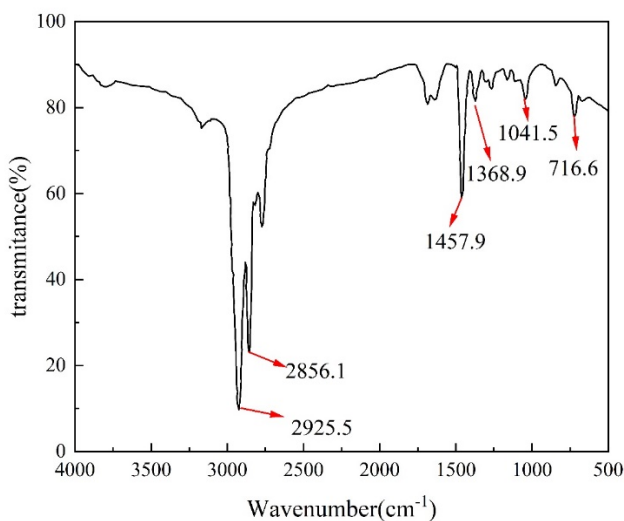


31 Octadecylamine (0.05 mol) and anhydrous ethanol (100 mL) were added to a three-necked
32 flask and stirred magnetically at 60 °C to dissolve completely. Then formic acid (0.215 mol) and
33 formaldehyde (0.215 mol) were added into the three-necked flask using a constant pressure titration
34 funnel at 90 °C, and the reaction was carried out for 2-3 h. After the reaction, the pH was adjusted
35 with standard NaOH solution to be greater than 10; after the solution was delaminated, the aqueous

36 phase was removed. The final product was taken out to be distilled under reduced pressure to remove
37 the unreacted formic acid and formaldehyde, and then finally obtained as a product, which was dried
38 in the oven at 50 °C.

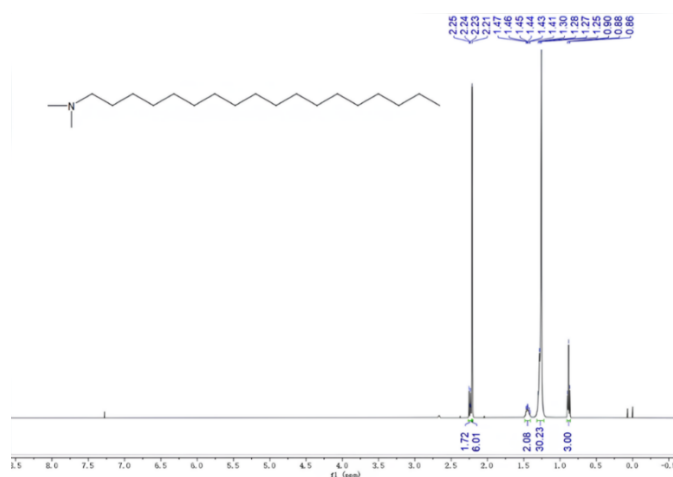
39 1.3. Structural characterization

40 The structure of DMA18 was confirmed by FTIR (Fig. IR) and ¹H-NMR (Fig. NMR). The
41 characteristic peaks were located at 2925.5 cm⁻¹ (-CH₃), 2856.1 cm⁻¹ (-CH₂-), 1457.9 cm⁻¹ (-C-
42 CH₃), 1041.5 cm⁻¹ (C-N). The ¹H-NMR of the synthesized product is shown in Fig. 2, which shows
43 that the synthesized product has hydrogen proton peaks at δ = 0.86~0.90 for -CH₃, δ = 1.25~1.30
44 for -CH₂-, and δ = 2.23~2.25 for hydrogen proton peaks on the N-neighboring position C of N-CH₂.
45 On the N-neighboring methyl group of N-CH₃ at δ = 2.21, and the hydrogen proton peak on the N-
46 interstitial C of N-CH₂-CH₂ at δ = 1.41~1.47. This result indicates that the synthesized product
47 conforms to the structural features of DMA18.



48
49

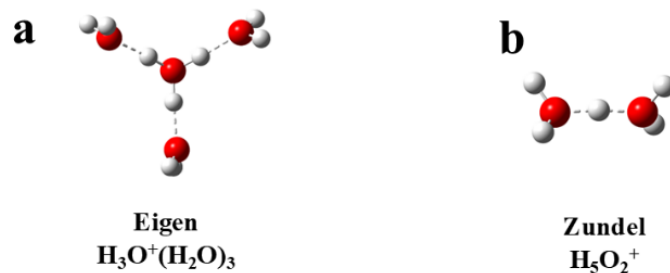
Fig. S1. Infrared spectrum of DMA18.



50
51
52

Fig. S2. ¹H NMR spectra data of DMA18

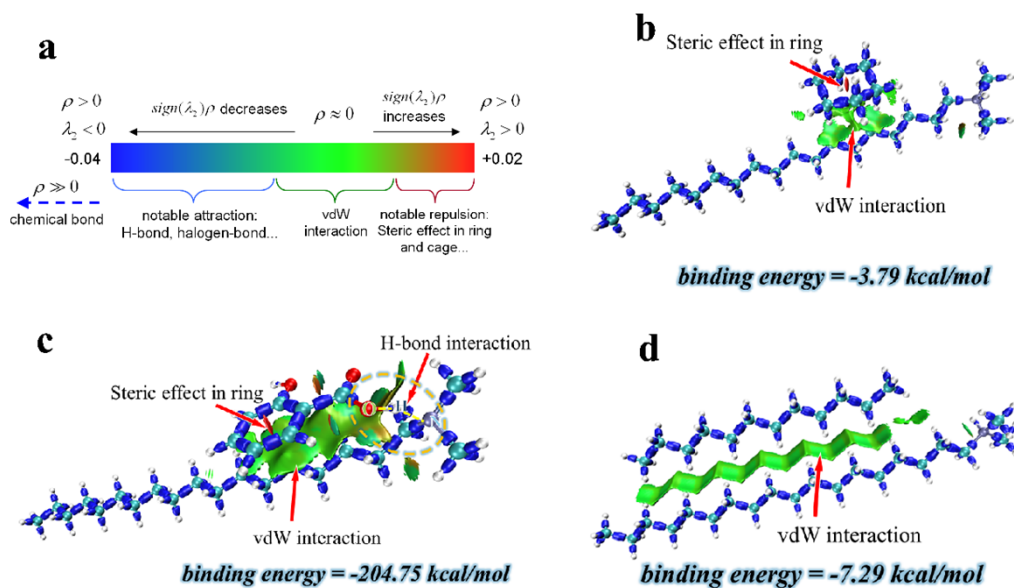
2. DFT calculation



53
54
55
56

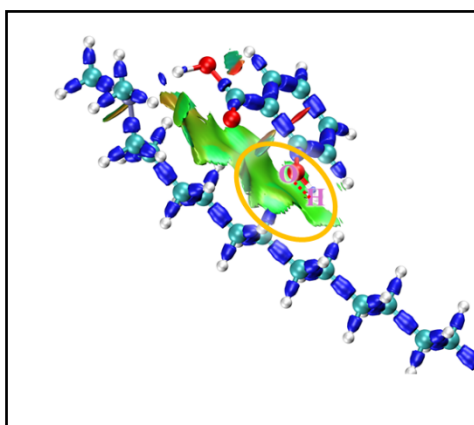
Fig. S3 Hydrated proton configuration

Weak interaction analyses were performed using the multiwfn program¹ for IRI analyses² and are shown in Fig. S4 and Fig. S5.



57
58
59
60

Fig. S4. Weak interaction IRI plots and interaction energies for (a) standard coloring method and chemical explanation of $\text{sign}(\lambda_2)\rho$ on IRI isosurfaces., (b) n-pentane and DMA18H+, (c) Sal- and DMA18H+, (d) dodecane and DMA18H+



61
62

Fig. S5 Weak interactions between phenolic hydroxyl groups of counterions Sal- and surfactants

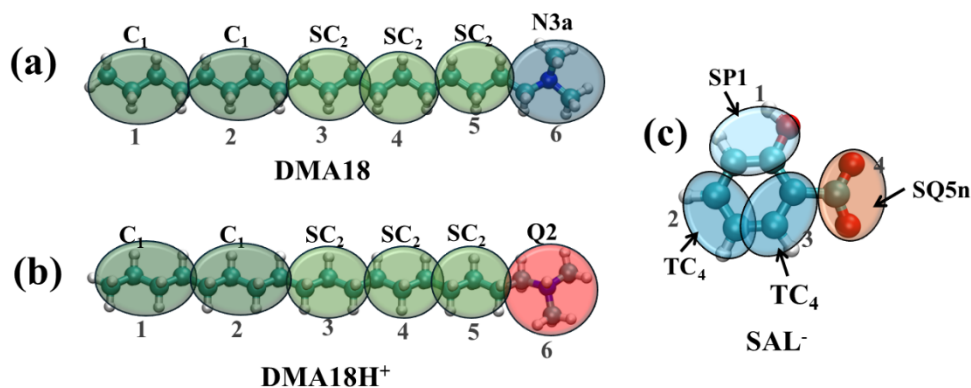
63 3. Model determination of molecular dynamics parameters for coarse-grained

64 All coarse-graining in this thesis was parameterized using the Martini 3.0.0 force field³. We
65 designed four coarse-graining schemes.

66 3.1 Coarse-grained Schemes 1

67 Fig. S6 is an exact match on all atoms of DMA18 with DMA18H⁺ according to the beads
68 defined by Souza et al.³, with C1 beads for four carbon atoms, SC2 beads for three carbon atoms,
69 and Q2 beads for the quaternary ammonium head group. By comparing the all-atom molecular
70 dynamics, it was found that the distribution of bond lengths between 3-4, 4-5, and 5-6 atom obtained
71 from the all-atom molecular dynamics of the DMA18 molecule was bimodal, which could not well
72 match the normal distribution obtained from the coarse-grained model, as shown in Fig. The same
73 situation occurs for the distribution pattern of the DMA18H⁺ ion. The structure of the model self-
74 assembled into spherical micelles was found by 1000 ns molecular dynamics simulations to be
75 inconsistent with the experimentally observed structure.

76 Scheme 1 follows the bead definition proposed by Souza et al. ³, where all atoms of DMA18
77 and DMA18H⁺ are perfectly matched. Four carbon atoms are represented by the C1 bead, three
78 carbon atoms by the SC2 bead, and the quaternary ammonium headgroup by the Q2 bead. Through
79 a comparison with all-atom molecular dynamics, it was found that the bond length distributions
80 between atoms 3-4, 4-5, and 5-6 of the DMA18 molecule obtained from CGMD simulations exhibit
81 a bimodal distribution, which does not match well with the normal distribution obtained from the
82 all-atom simulations, as shown in the Fig. S7. The distribution pattern of DMA18H⁺ ions also
83 exhibits this behavior. Additionally, Molecular dynamics simulations over 1000 ns revealed that the
84 self-assembled spherical micelle structure obtained from this model does not match the
85 experimentally observed worm-like micelle structure.



86

87 Fig. S6 coarse-grained model for schemes 1. (a) DMA18 coarse-grained model, (b) coarse-
88 graining model of DMA18H⁺ after DMA18 response to CO₂, and (c) coarse-grained model of
89 counterions Salicylate ion (Sal⁻).

90

91

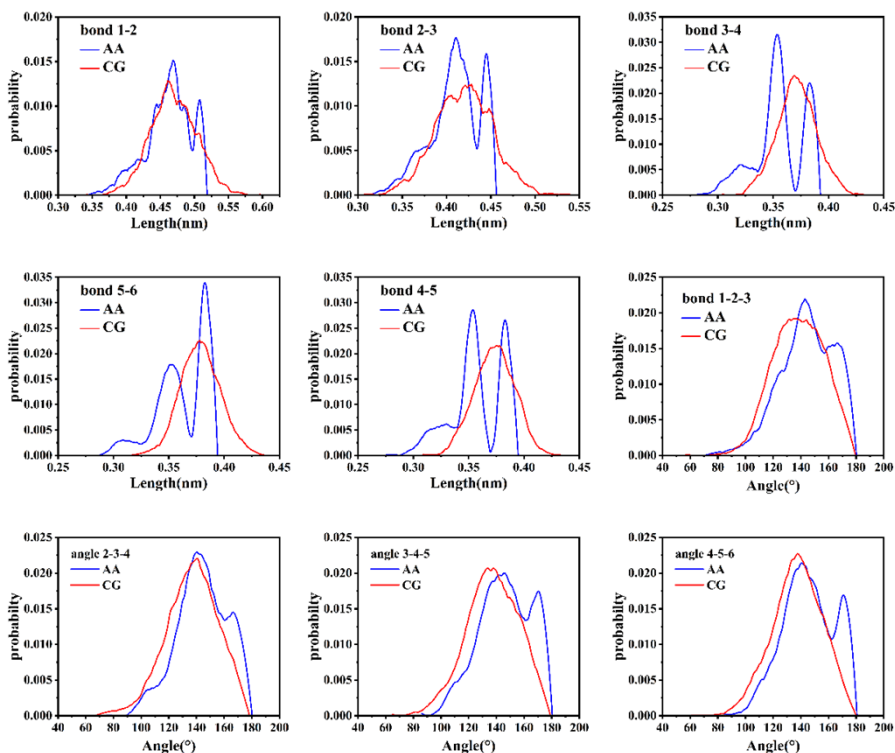
92

93 Table S1

	Bond parameters			Angle parameters		
	Bond	R_0	$K_{\text{stretch}}(\text{kJ} \cdot \text{mol}^{-1} \cdot \text{nm}^{-2})$	Angle	$\theta_0(^{\circ})$	$K_{\text{bend}}(\text{kJ} \cdot \text{mol}^{-1})$
DMA18	1-2	0.481	2200	1-2-3	164	24
	2-3	0.429	2400	2-3-4	163	24
	3-4	0.375	8000	3-4-5	166	24
	4-5	0.376	8000	4-5-6	165	22
	5-6	0.381	8000	-	-	-
C18DAH ⁺	1-2	0.472	2200	1-2-3	163	24
	2-3	0.430	2400	2-3-4	164	24
	3-4	0.370	8000	3-4-5	168	24
	4-5	0.370	8000	4-5-6	166	22
	5-6	0.369	8000	-	-	-
Sal ⁻	1-2	0.210	constraints	-	-	-
	2-3	0.229	constraints	-	-	-
	3-4	0.267	constraints	-	-	-
	2-4	0.218	50000			

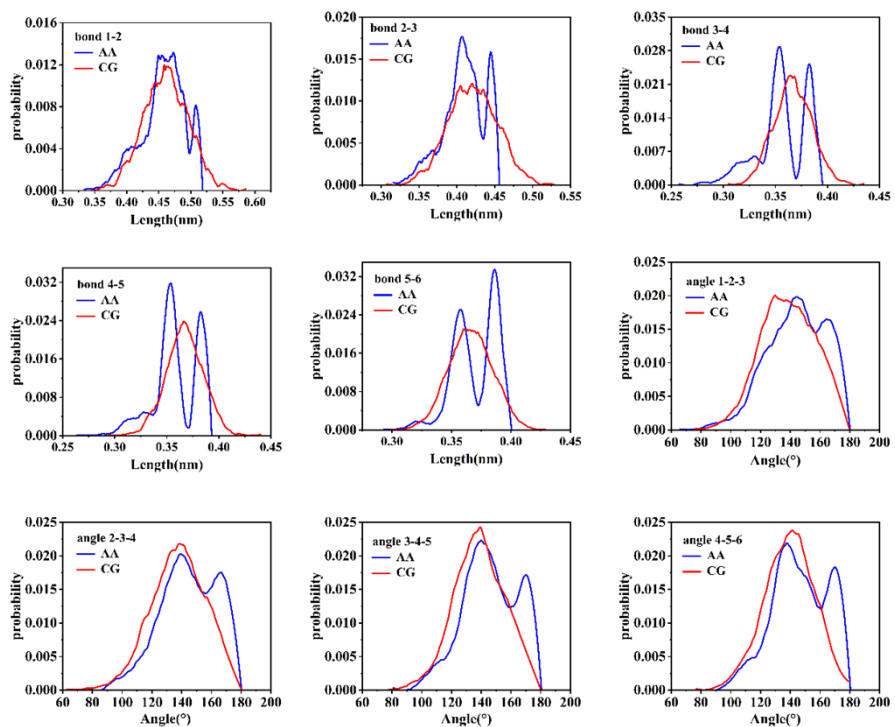
94

95



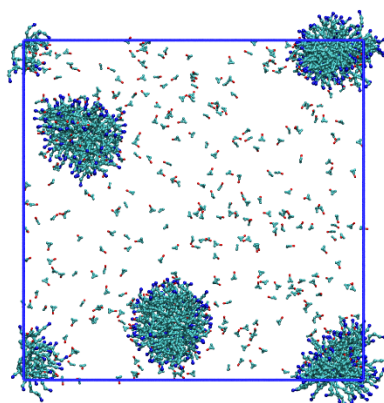
96

97 Fig. S7. Coarse-grained Scheme 1, Bond length and bond angle distributions of DMA18
 98 molecules from all-atom molecular dynamics and coarse-grained molecular dynamics simulations.



99

100 Fig. S8. Coarse-grained Scheme 1, Bond length and bond angle distributions of DMA18H+
 101 molecules from all-atom molecular dynamics and coarse-grained molecular dynamics simulations.

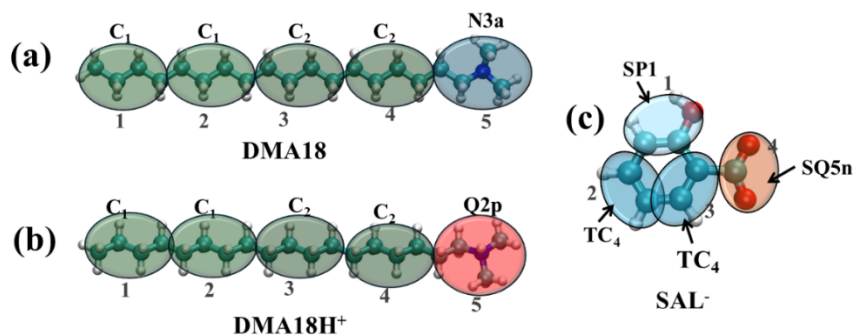


102

103 Fig. S9 Self-assembly of DMA18H⁺ with the counterions Sal⁻ for coarse-grained Schemes 1

104 3.2 Coarse-grained Schemes 2

105 Scheme 2 also follows the rules defined by Souza et al.³ using beads of type “R” to match
 106 atoms, with C1 beads for carbon atoms near the hydrophobic tail chain and C2 beads for carbon
 107 atoms between hydrophobic chain segments. In order to more accurately represent the quaternary
 108 charge off-domain phenomenon after protonation, the Q2 beads were labeled with “q”³.
 109 Counterions Sal⁻ using the coarse mechanics model from schemes 1. The statistics of bond length
 110 and bond angle distributions by all-atom molecular dynamics and coarse-grained molecular
 111 dynamics show that the coarse-grained scheme matches the bond length and bond angle
 112 distributions obtained by all-atom molecular dynamics more closely compared to the coarse-grained
 113 scheme of schemes 1. coarse-grained molecular dynamics simulated 1000 ns. However, the worm-
 114 like micelle structure was still not captured.



115

116 Fig. S10. Structure of Coarse-grained schemes 2.

117

118

119

120

121

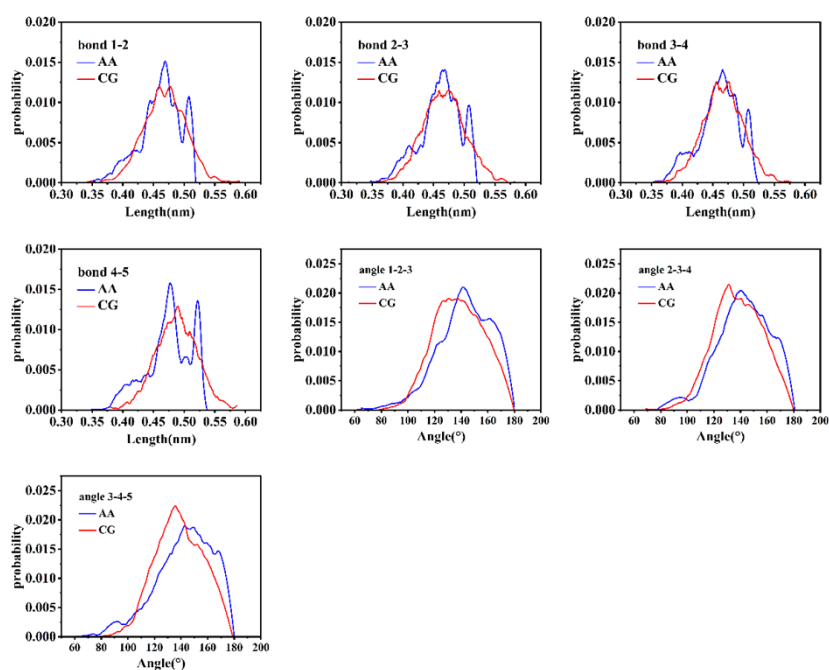
122

123

124

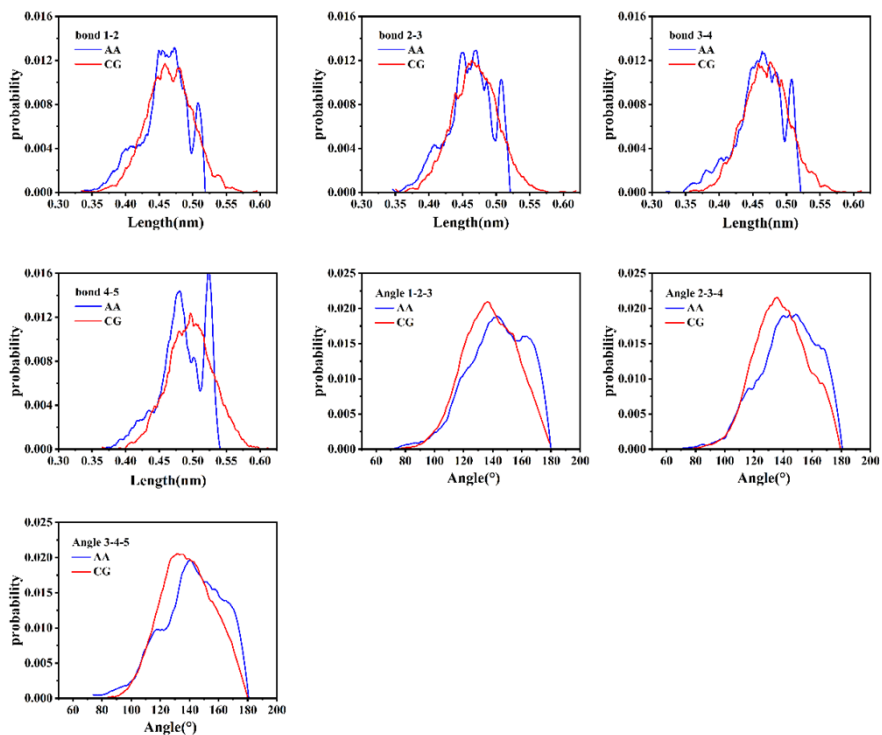
	Bond parameters			Angle parameters		
	Bond	R_0	$K_{\text{stretch}}(\text{kJ} \cdot \text{mol}^{-1} \cdot \text{nm}^{-2})$	Angle	$\theta_0(^{\circ})$	$K_{\text{bend}}(\text{kJ} \cdot \text{mol}^{-1})$
DMA18	1-2	0.481	2200	1-2-3	164	24
	2-3	0.429	2400	2-3-4	163	24
	3-4	0.375	8000	3-4-5	166	24
	4-5	0.376	8000	-	-	-
C18DAH ⁺	1-2	0.476	2200	1-2-3	162	24
	2-3	0.480	2200	2-3-4	163	24
	3-4	0.480	2200	3-4-5	161	24
	4-5	0.503	2200	-	-	-
Sal ⁻	1-2	0.210	constraints	-	-	-
	2-3	0.229	constraints	-	-	-
	3-4	0.267	constraints	-	-	-
	2-4	0.200	50000	-	-	-

126



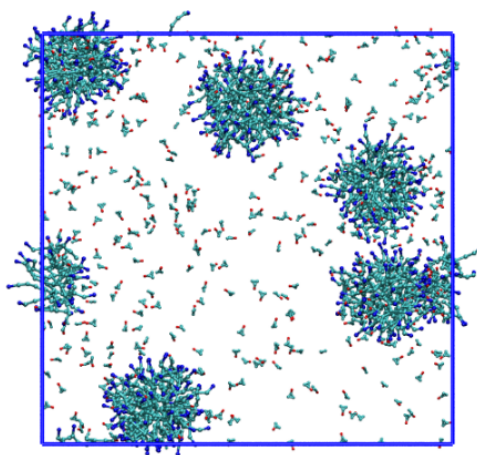
127

128 Fig. 11. Coarse-grained Scheme 2, Bond length and bond angle distributions of DMA18H+
 129 molecules from all-atom molecular dynamics and coarse-grained molecular dynamics simulations.



130

131 Fig. S12. Coarse-grained Scheme 2, Bond length and bond angle distributions of DMA18H+
 132 molecules from all-atom molecular dynamics and coarse-grained molecular dynamics simulations.



133

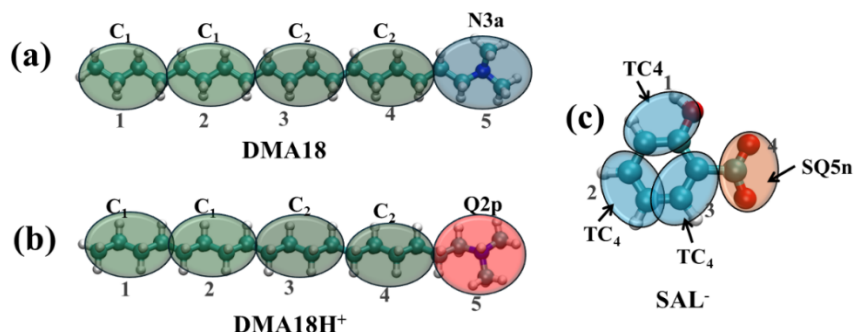
134

135 Fig. S13. Self-assembly of DMA18H+ with the counterions Sal- for coarse-grained Schemes 2

136 3.3 Coarse-grained Schemes 3

137 Scheme 3 builds upon Scheme 2, where we improved the coarse-grained model for Sal- ions
 138 by replacing the bead at position 1 in the Sal- model with a TC4 bead. After performing a 1000 ns
 139 simulation, it was observed that the micelles showed a tendency to grow into worm-like micelles.
 140 This suggests that the phenolic hydroxyl group cannot be simplified to an ethanol bead, likely due

141 to the conjugation effect of the benzene ring, which weakens the polarity of the hydroxyl group and
 142 increases its hydrophobicity. We then extended the simulation by another 1000 ns, and the results
 143 showed that the worm-like micelles did not continue to grow. At this point, the maximum number
 144 of DMA18H⁺ ions in the micelles was 189, indicating that the system had reached a stable state.



145

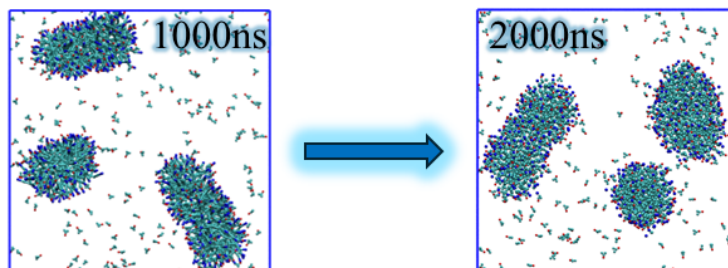
146

Fig. S14 Structure of Coarse-grained Schemes 3

147 Table S3

	Bond parameters			Angle parameters		
	Bond	R ₀	K _{stretch} (kJ · mol ⁻¹ · nm ⁻²)	Angle	θ ₀ (°)	K _{bend} (kJ mol ⁻¹)
DMA18	1-2	0.481	2200	1-2-3	164	24
	2-3	0.429	2400	2-3-4	163	24
	3-4	0.375	8000	3-4-5	166	24
	4-5	0.376	8000	-	-	-
C18DAH ⁺	1-2	0.476	2200	1-2-3	162	24
	2-3	0.480	2200	2-3-4	163	24
	3-4	0.480	2200	3-4-5	161	24
	4-5	0.503	2200	-	-	-
Sal ⁻	1-2	0.210	constraints	-	-	-
	2-3	0.229	constraints	-	-	-
	3-4	0.267	constraints	-	-	-
	2-4	0.200	14000	-	-	-

148

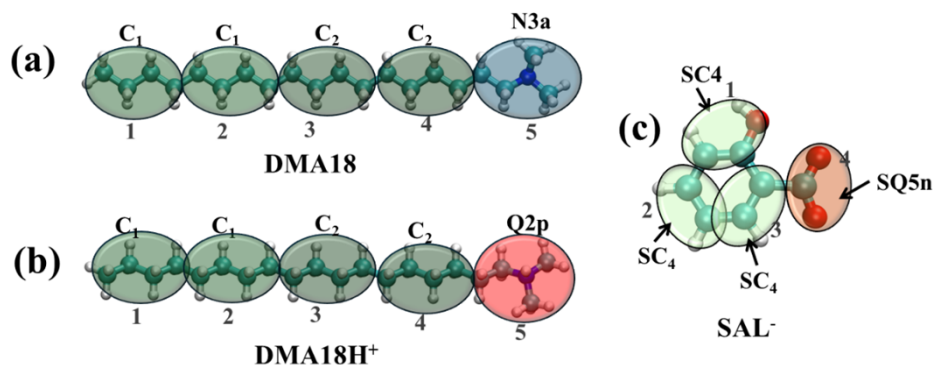


149

150 Fig. S15. Self-assembly of DMA18H⁺ molecules after 2000 ns of simulation with coarse-grained
 151 Scheme 3.

152 3.4 Coarse-grained Schemes 4

153 From the above simulations, we found that increasing the hydrophobicity of the salicylate
 154 sodium benzene ring bead can promote the self-assembly of surfactants into worm-like micelles.
 155 Therefore, based on coarse-grained Scheme 3, we replaced the TC4 bead of Sal⁻ with the SC4 bead,
 156 a modification widely used in the Martini 2.0 version, which has shown good results in various
 157 studies⁴⁻⁶. According to Souza's definition³, the SC4 bead exhibits stronger hydrophobicity than the
 158 TC4 bead. After performing a 1000 ns coarse-grained molecular dynamics simulation, we found
 159 that the worm-like micelles were more pronounced compared to Scheme 3. Further extending the
 160 simulation by an additional 1000 ns, the maximum number of DMA18H⁺ ions in the micelles
 161 increased to 319, suggesting that this system is more suitable for coarse-grained model simulations.
 162 In conclusion, by optimizing the coarse-graining of the Sal⁻ benzene ring structure, we found that
 163 the stronger the hydrophobicity of the benzene ring, the more easily the system self-assembles into
 164 worm-like micelles. Therefore, using more hydrophobic counterions such as sodium p-
 165 toluenesulfonate or sodium p-styrenesulfonate may yield even better results.



166

167

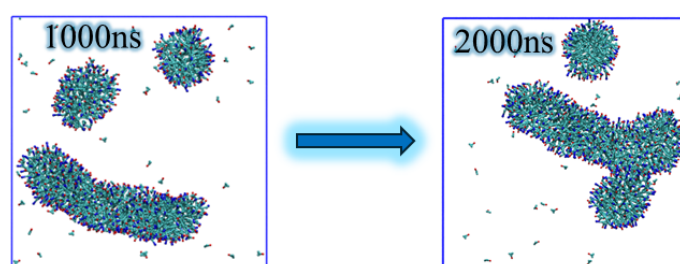
Fig. S16 Structure of Coarse-graining Scheme 4

168 Table S4

		Bond parameters		Angle parameters		
DMA18	Bond	R ₀	K _{stretch} (kJ · mol ⁻¹ · nm ⁻²)	Angle	θ ₀ (°)	K _{bend} (kJ · mol ⁻¹)

	1-2	0.481	2200	1-2-3	164	24
	2-3	0.429	2400	2-3-4	163	24
	3-4	0.375	8000	3-4-5	166	24
	4-5	0.376	8000	-	-	-
C18DAH ⁺	1-2	0.476	2200	1-2-3	162	24
	2-3	0.480	2200	2-3-4	163	24
	3-4	0.480	2200	3-4-5	161	24
	4-5	0.503	2200	-	-	-
Sal ⁻	1-2	0.210	constraints	-	-	-
	2-3	0.229	constraints	-	-	-
	3-4	0.267	constraints	-	-	-
	2-4	0.200	14000			

169

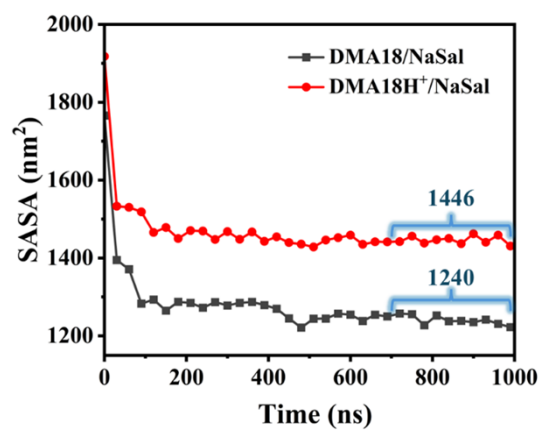


170

171 Fig. S17 Self-assembly of DMA18H⁺ molecules after coarse-graining Schemes 4, 1000 to 2000 ns.
172

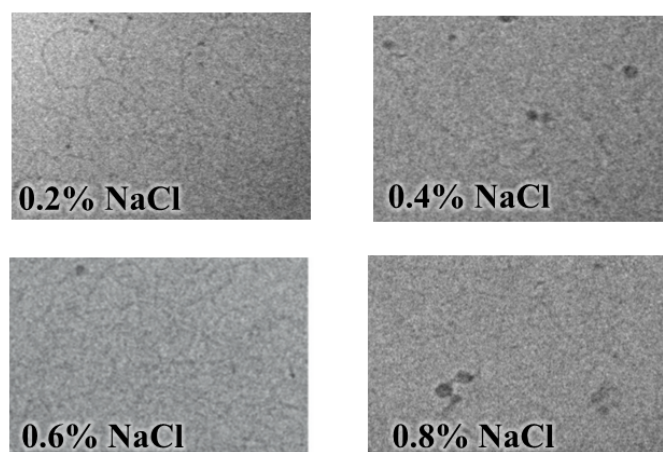
173 4. Molecular dynamics analysis of CGMD

174 The hydrophobic interaction results in a decrease in the contact area of the surfactant
175 hydrophobic tail chain with water ⁷. Therefore, changes in hydrophobic interactions can be
176 responded to by changes in the solvent accessible surface area (SASA) of the surfactant hydrophobic
177 tail chain with water. As shown in Fig. S18, the solvent-accessible surface area change of 100 mM
178 DMA18/NaSal system versus 100 mM DMA18H⁺/NaSal system, DMA18 and DMA18H⁺ rapidly
179 aggregated, and the solvent-accessible surface area rapidly decreased. Averaging the last 300 ns,
180 the solvent-accessible surface area of the DMA18H⁺/NaSal system was 1446 nm², and the solvent-
181 accessible surface area of the DMA18/NaSal system was 1240 nm².



182

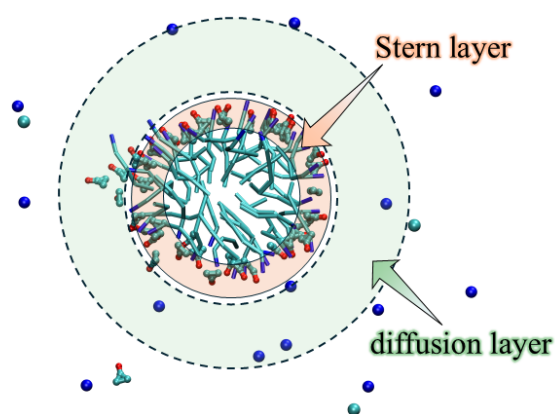
183 Fig. S18 Solvent-accessible surface area (SASA) of aggregates of the DMA18/NaSal system vs.
 184 the DMA18H⁺/NaSal system.



185

186

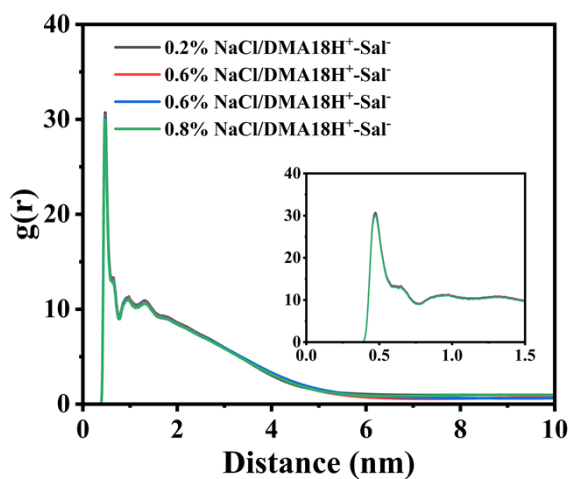
Fig S19 Cryo-TEM with different Salt concentrations



187

188

Fig. S20 Worm-like micelle cross-section



189

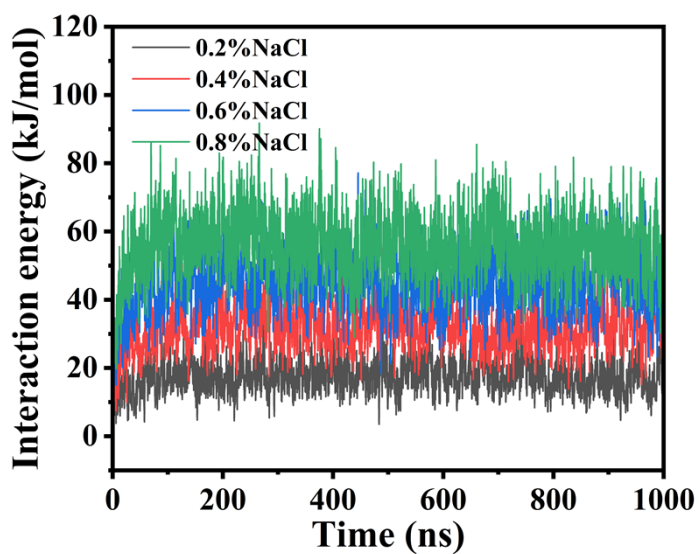
190 Fig. S21 Radial distribution function between DMA18H⁺ and Sal⁻ ions at different NaCl
 191 concentrations.

192 Table S5

System	0.2%NaCl	0.4%NaCl	0.6%NaCl	0.8%NaCl
SASA(nm ²)	1602.0	1607.5	1606.0	1619.3

193

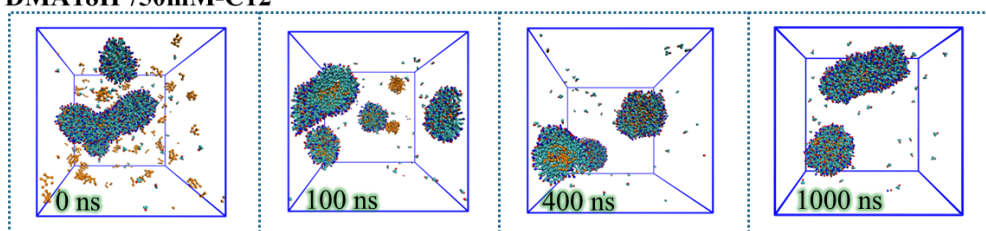
194



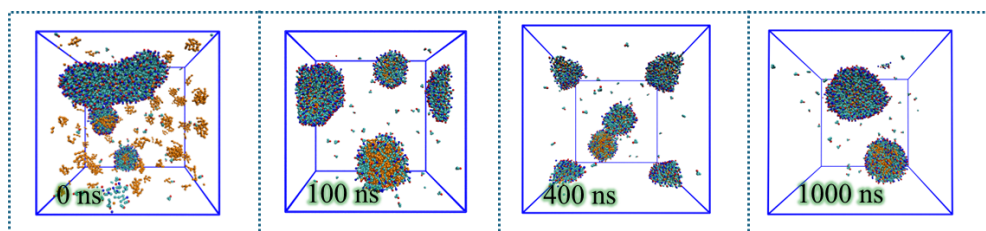
195

196 Fig. S22 Interaction energy between Na⁺ ions and DMA18H⁺ ions at different Salt concentrations.

(a) DMA18H⁺/50mM-C12

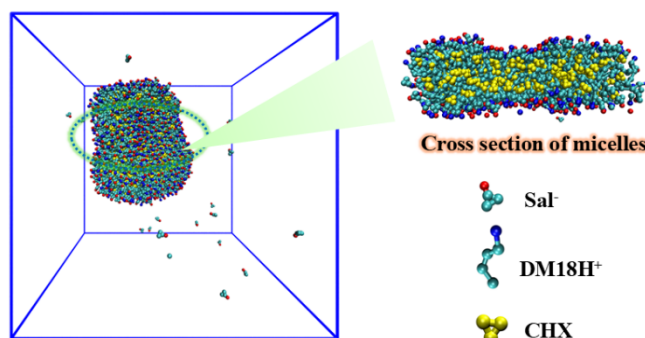


(b) DMA18H⁺/100mM-C12



197
198
199
200

Fig. S23 Self-assembly of C12-containing worm-like micellar systems, (a) C12 concentration of 50 mM system, (b) C12 concentration of 100 mM system



201
202
203
204

Fig. S24 Self-assembly of worm-like micellar systems containing cyclopentane (CHX)

References

- 205 1 T. Lu and F. Chen, *Journal of Computational Chemistry*, 2012, 33, 580–592.
206 2 T. Lu and Q. Chen, *Chemistry–Methods*, 2021, 1, 231–239.
207 3 P. C. T. Souza, R. Alessandri, J. Barnoud, S. Thallmair, I. Faustino, F. Grünewald, I. Patmanidis,
208 H. Abdizadeh, B. M. H. Bruininks, T. A. Wassenaar, P. C. Kroon, J. Melcr, V. Nieto, V. Corradi,
209 H. M. Khan, J. Domański, M. Javanainen, H. Martinez-Seara, N. Reuter, R. B. Best, I. Vattulainen,
210 L. Monticelli, X. Periole, D. P. Tieleman, A. H. de Vries and S. J. Marrink, *Nat Methods*, 2021,
211 18, 382–388.
212 4 A. V. Sangwai and R. Sureshkumar, *Langmuir*, 2011, 27, 6628–6638.

- 213 5 P. Wang, S. Pei, M. Wang, Y. Yan, X. Sun and J. Zhang, *Journal of Colloid and Interface Science*,
214 2017, 494, 47–53.
- 215 6 S. Dhakal and R. Sureshkumar, *ACS Macro Lett.*, 2016, 5, 108–111.
- 216 7 D. Chandler, *Nature*, 2005, 437, 640–647.
- 217